Journal of Pharmaceutical Analysis 14 (2024) 321–334

Contents lists available at ScienceDirect

Journal of Pharmaceutical Analysis

journal homepage: www.elsevier.com/locate/jpa

Original article

Enhancing metformin-induced tumor metabolism destruction by glucose oxidase for triple-combination therapy

Rangrang Fan [a, 1], Linrui Cai [b, 1], Hao Liu [a], Hongxu Chen [a], Caili Chen [c], Gang Guo [a, **], Jianguo Xu [a, *]

[a] Department of Neurosurgery and Institute of Neurosurgery, Cancer Center and State Key Laboratory of Biotherapy, West China Hospital, Sichuan University, Chengdu, 610041, China
[b] NMPA Key Laboratory for Technical Research on Drug Products in Vitro and in Vivo Correlation, Key Laboratory of Birth Defects and Related Diseases of Women and Children of MOE, National Drug Clinical-Trial Institution, West China Second Hospital, Sichuan University, Chengdu, 610041, China
[c] Department of Immunology, School of Basic Medical Sciences, Xinxiang Medical University, Xinxiang, Henan, 453000, China

ARTICLE INFO

Article history:
Received 16 June 2023
Received in revised form
18 September 2023
Accepted 19 September 2023
Available online 23 September 2023

Keywords:
Metformin
Glucose oxidase
Metabolism disruption
Tumor starvation
Combination cancer therapy

ABSTRACT

Despite decades of laboratory and clinical trials, breast cancer remains the main cause of cancer-related disease burden in women. Considering the metabolism destruction effect of metformin (Met) and cancer cell starvation induced by glucose oxidase (GOx), after their efficient delivery to tumor sites, GOx and Met may consume a large amount of glucose and produce sufficient hydrogen peroxide *in situ*. Herein, a pH-responsive epigallocatechin gallate (EGCG)-conjugated low-molecular-weight chitosan (LC-EGCG, LE) nanoparticle (Met–GOx/Fe@LE NPs) was constructed. The coordination between iron ions (Fe^{3+}) and EGCG in this nanoplatform can enhance the efficacy of chemodynamic therapy via the Fenton reaction. Met–GOx/Fe@LE NPs allow GOx to retain its enzymatic activity while simultaneously improving its stability. Moreover, this pH-responsive nanoplatform presents controllable drug release behavior. An *in vivo* biodistribution study showed that the intracranial accumulation of GOx delivered by this nanoplatform was 3.6-fold higher than that of the free drug. The *in vivo* anticancer results indicated that this metabolism destruction/starvation/chemodynamic triple-combination therapy could induce increased apoptosis/death of tumor cells and reduce their proliferation. This triple-combination therapy approach is promising for efficient and targeted cancer treatment.

1. Introduction

Breast cancer is the most commonly diagnosed cancer in women (nearly 30%) worldwide, with millions of people suffering from the disease each year [1]. Through significant therapeutic advances, the relative survival rates of most patients are high, although advanced breast cancer patients with distant metastasis have a poor 5-year survival rate [2]. Similar to most cancers, breast cancer shows metabolic adaptability consistent with the Warburg effect, including increased glucose uptake and glycolytic activity, to ensure adequate levels of adenosine 5′-triphosphate (ATP) for the demands of rapid tumor proliferation, maintenance, and malignant progression [2,3]. Compared with normal cells, the observed Warburg effect in cancer cells has promoted the establishment of innovative methods targeting glycolysis for antitumor therapy.

Metformin (Met), a classic drug for type 2 diabetes mellitus, has been proven to hinder glycolysis and decrease ATP production and tumor cell oxygen (O_2) consumption by inhibiting the catalytic formation of phosphorylated glucose and the mitochondrial electron transport chain [4,5]. Benefiting from this, Met has also been identified as a unique anticancer agent that curbs tumor development and improves the prognosis of patients [6]. However, the therapeutic effects of Met alone on cancer metabolism are highly dose-dependent and saturable due to the intracellular accumulation of glucose and insulin, which blocks glucose metabolic pathways [7]. To enhance the antitumorigenic role of Met, it is necessary to deplete the accumulated intracellular glucose using a combination treatment strategy. Glucose oxidase (GOx), an endogenous oxidoreductase, can effectively catalyze intracellular glucose in the presence of O_2 to produce gluconic acid and hydrogen peroxide

Peer review under responsibility of Xi'an Jiaotong University.
* Corresponding author.
** Corresponding author.
E-mail addresses: guogang@scu.edu.cn (G. Guo), xujg@scu.edu.cn (J. Xu).
[1] Both authors contributed equally to this work.

https://doi.org/10.1016/j.jpha.2023.09.015

(H_2O_2) [8]. Given its crucial role in glucose oxidation and its ability to halt the necessary nutrient supply to cancer cells, GOx-based synergistic therapy has attracted much attention [9,10]. It has been predicted that combining GOx therapy with Met administration could lead to the consumption of intracellular glucose and the production of toxic H_2O_2 to effectively kill tumor cells. Moreover, Met-induced O_2 deposition at tumor sites can in turn increase the catalytic activity of GOx [4,11,12]. Unfortunately, the poor absorption, short half-life, and high rate of degradation of GOx hamper its clinical application and transformation.

Hence, efficiently delivering GOx and Met to tumor sites with rationally designed nanocarriers will further enhance their therapeutic efficiency by hampering glycolysis and supplying strong oxidizing free radicals *in situ*. Many natural and synthetic materials have been explored for drug delivery [13,14]. Among them, chitosan (CS), derived by deacetylating chitin, has attracted much attention in drug delivery due to its biodegradability, biocompatibility, bioadhesion, and nontoxicity [15–17]. In addition, CS is a weak polybase with a pKa of approximately 6.5, which means that in a physiological environment with a pH above 6.5, CS will not be protonated. This allows CS to protect drugs from degradation during administration, resulting in a prolonged half-life and greater bioavailability of the drug [16,18]. The amino groups of CS are positively charged at pH 6.5, implying that an electrostatic interaction between CS-based nanocarriers and negatively charged biological membranes can occur, resulting in enhanced endocytosis by cells [19–21]. Considering that the low water dispersibility of CS will hinder its further application in the biomedical field, there is an urgent need to develop water-soluble CS-based derivatives.

The abundant amino groups on its backbone allow CS to be easily modified through moderate cross-linking reactions [22]. Epigallocatechin gallate (EGCG), a natural polyphenol extracted from green tea that possesses reactive catechol groups, has recently been widely explored for the synthesis of EGCG-conjugated polymeric networks [23,24]. Specifically, the abundant hydroxyl groups and aromatic groups on EGCG can endow it with a strong binding affinity for proteins, peptides, nucleic acids, and metal ions, which can expedite the assembly of nanostructures and further attachment to cell surfaces [25,26]. Moreover, the anticancer effect of EGCG has been proven in epidemiological, preclinical, and clinical studies [27]. Inspired by this, low-molecular-weight CS (LC) was modified with EGCG to synthesize the LC-EGCG (LE) conjugate, and then a pH-responsive nanoparticle (Met–GOx/Fe@LE NPs) based on Met and GOx was constructed for metabolism destruction/starvation/chemodynamic triple-combination therapy. The coordination between iron ions (Fe^{3+}) and EGCG in this nanoplatform can enhance the efficacy of chemodynamic therapy via the Fenton reaction [28,29]. Taking advantage of the CS modification, the Met–GOx/Fe@LE NPs efficiently accumulated in tumor cells and initiated the release of the Met/GOx combination into the tumor cytoplasm. This design strategy can protect GOx from enzyme degradation and enhance the antitumorigenic role of Met by depleting the accumulated intracellular glucose (Fig. 1). Moreover, damage to healthy tissue can be minimized and higher therapeutic efficacy can be achieved, as evidenced by slower tumor growth, increased tumor cell apoptosis and decreased liver metastasis.

2. Materials and methods

2.1. Materials

LC (molecular weight 50–190 kDa, with a deacetylation degree of 75%–85%) was obtained from Sigma-Aldrich (St. Louis, MO, USA). GOx (Cat# G109029, >180 U/mg), Met (Cat# 1115-70-4), L-ascorbic acid, NaOH, acetic acid, 30% (*V*/*V*) H_2O_2, and methylene blue (MB) were all purchased from Aladdin Reagent Ltd. (Shanghai, China). EGCG (Cat# MB1672, ≥95%) and calcein acetoxymethyl ester (calcein-AM)/propidium iodide (PI) (Cat# MA0361) were purchased from Dalian Meilun Biotechnology Co., Ltd. (Dalian, China). AKT, p-AKT, and cleaved caspase 9 antibodies were obtained from Huabio (Hangzhou, China). The annexin V-fluorescein isothiocyanate (FITC)/7-amino-actinomycin D (7AAD) apoptosis detection kit (Cat# FXP018) was purchased from Beijing 4A Biotech Co., Ltd. (Beijing, China). Phosphate-buffered saline (PBS), 4′,6-diamidino-2-phenylindole (DAPI), Hoechst 33342, radioimmunoprecipitation assay (RIPA) lysis buffer, and a bicinchoninic acid (BCA) kit were obtained from Beyotime Biotechnology (Shanghai, China).

2.2. Synthesis and characterization of the LE conjugate

The LE conjugate used in this study was synthesized according to the methods of Lei et al. [30]. Briefly, 100 mL of CS solution (0.5%, *m*/*V*) in a 150 mL glass flask was adjusted to pH 3.5 with NaOH (10 M), followed by the addition of 1 mL of H_2O_2 (0.5 M) containing ascorbic acid (0.025 g). After stirring for 1 h, EGCG was added, and the solution was allowed to react for 12 h with magnetic stirring at 40 °C. The resulting solution was dialyzed (molecular weight cut-off: 14,000 Da; Millipore, Billerica, MA, USA) for 72 h and then lyophilized to obtain the LE conjugate. The ^{1}H nuclear magnetic resonance (^{1}H NMR) spectrum of LE was recorded on a Bruker Avance III 400 M instrument (Bruker, Frankfurt, German) at 400 MHz using D_2O as the solvent. Fourier transform infrared (FTIR) spectra and ultraviolet visible (UV-vis) absorption spectra of LC, EGCG, and LE were obtained with a Nicolet™ iS50 FTIR instrument (Thermo Fisher Scientific Inc., Waltham, MA, USA) and a UV-vis spectrophotometer (UV-2550; Shimadzu, Kyoto, Japan), respectively.

2.3. Preparation and characterization of Met–GOx/Fe@LE NPs

Met- and GOx-loaded LE NPs (Met–GOx/Fe@LE NPs) were prepared by the probe supersonic method. Briefly, 50 μL of $FeCl_3$ (20 mM) was added dropwise to 850 μL of LE aqueous solution (containing 2 mg of LE) with a probe sonicator (XINYI-IID, Xinyi Ultrasonic Equipment Co., Ltd., Ningbo, China). Then, 50 μL of GOx solution (10 mg/mL) and 50 μL of Met solution (10 mg/mL) were added under the same conditions to prepare Met–GOx/Fe@LE NPs. The particle size and morphology of the Met–GOx/Fe@LE NPs were examined using dynamic light scattering (DLS; Malvern, Melvin, UK) and transmission electron microscopy (TEM; Hitachi HT7800, Tokyo, Japan), respectively. Blank Fe@LE NPs and NPs loaded with Met (Met/Fe@LE NPs) or GOx (GOx/Fe@LE NPs) alone were prepared using a similar method. To determine the optimal concentration of LE and Fe^{3+}, the volumes of $FeCl_3$ (50 μL) and the LE aqueous solution (850 μL) were fixed. A series of Fe@LE NPs were obtained by varying the final concentrations of LE (0.5, 1.0, 2.0, 3.0, and 4.0 mg/mL) and Fe^{3+} (5, 10, 20, 30, and 40 mM). To further optimize the sonication intensity, the concentration of Fe^{3+} (20 mM) was fixed, and the particle size was measured after different sonication times (10, 30, 60, and 90 s).

The Met–GOx/Fe@LE NPs were washed, dispersed in saline, and stored at 4 °C for future use. The amounts of GOx and Met in the supernatant were analyzed by BCA assay kits and high-performance liquid chromatography (HPLC; Agilent 1260, Baden-Württemberg, Germany), respectively. The successful loading of GOx into the Met–GOx/Fe@LE NPs was further characterized by sodium dodecyl sulfate-polyacrylamide gel electrophoresis (SDS-PAGE). Typically, free GOx and Met–GOx/Fe@LE NPs (40 μL) were mixed with 10 μL of SDS-PAGE loading buffer, and 20 μL was loaded into the sample well on a 10% SDS-PAGE gel. Finally, the obtained

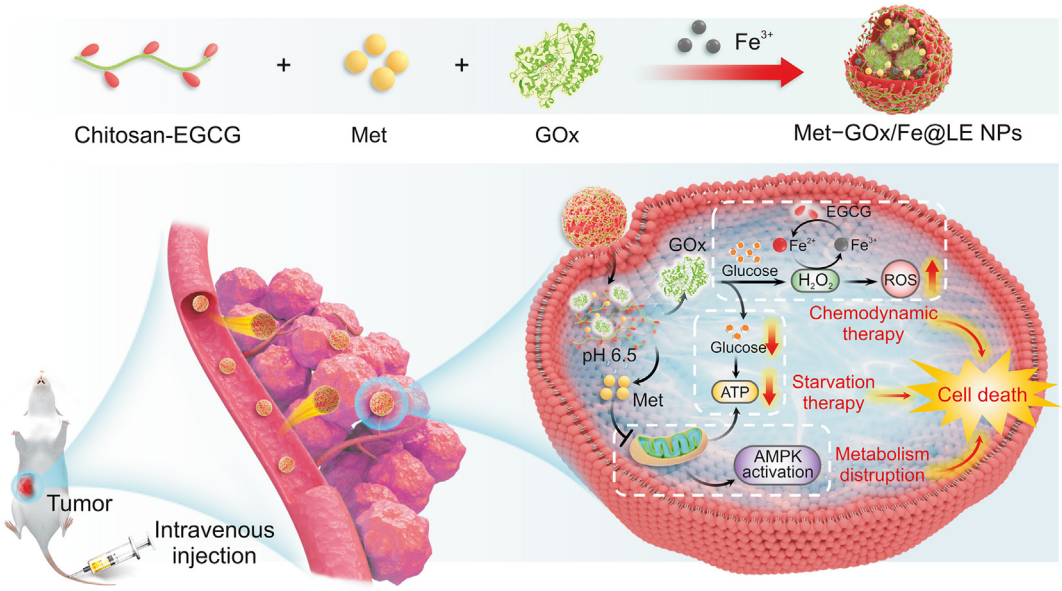

Fig. 1. Schematic illustration of metformin (Met)–glucose oxidase (GOx)/Fe@epigallocatechin gallate (EGCG)-conjugated low-molecular-weight chitosan (LC-EGCG, LE) nanoparticles (NPs)-mediated multiple mechanism-enhanced efficient cancer treatment. ROS: reactive oxygen species; ATP: adenosine triphosphate; AMPK: adenosine monophosphate-activated protein kinase.

SDS-PAGE gel was immersed in Coomassie brilliant blue solution to stain for 30 min and washed to observe the protein bands. The drug loading (DL) and encapsulation efficiency (EE) were determined as follows.

DL = (Weight of drug loaded in NPs)/(total weight of NPs) × 100%

EE = (Weight of drug loaded in NPs)/(weight of drug initially added) × 100%

For the molecular modeling study, theoretical calculations were performed with the Gaussian 16 program based on density functional theory (DFT). The structures of the studied molecules were fully optimized using the B3LYP functional with DFT-D3BJ dispersion correction combined with the 6-31 G* basis set [31]. The vibrational frequencies of the optimized structures were determined at the same level.

To investigate pH-responsive drug release, 0.5 mL of Met–GOx/Fe@LE NPs was placed in a dialysis bag and immersed in 10 mL of PBS (pH 5.4, 6.8, or 7.4) with continuous shaking at 37 °C. At different time intervals, 1 mL of the solution was removed, and 1 mL of fresh saline was added back. The amounts of Met and GOx released were determined as mentioned above.

2.4. Assays of catalytic and enzyme activities

GOx, GOx/Fe@LE NPs, and Met–GOx/Fe@LE NPs were incubated with different concentrations of glucose (0–400 μg/mL) at room temperature to determine their ability to deplete glucose catalytically. Then, the production of H_2O_2 was detected by using an H_2O_2 assay kit (Cat# BC3595; Solarbio, Beijing, China) according to previous studies [11,32].

Enzyme activity was determined according to our previous study [32]. Briefly, the working solution was prepared by mixing 0.2 mL of horseradish peroxidase (HRP) (0.179 mg/mL), 4.8 mL of dianisidine (0.14 mg/mL), and 1.0 mL of glucose (306.27 mg/mL). Then, 200 μL of the working solution and 10.0 μL of GOx, GOx/Fe@LE NPs, or Met–GOx/Fe@LE NPs (final concentration of GOx, 20 mU/mL) were added to a 96-well plate for 15 min of incubation, and then the absorbance was measured at 460 nm. The enzymatic activity was positively correlated with the slope of the absorbance curve. Then, the catalytic activity of the GOx in the nanoparticles was measured under different pH conditions.

2.5. Study of •OH generation

The ability of Met–GOx/Fe@LE NPs to generate ·OH in PBS (pH 5.4 and 7.4) was determined using MB as an indicator according to previous studies [33,34]. In brief, GOx, Fe@LE NPs, GOx/Fe@LE NPs, and Met–GOx/Fe@LE NPs (an equivalent GOx concentration of 50 μg/mL and Fe concentration of 200 μM) were mixed in PBS containing 0.3 mg/mL glucose and 10 μg/mL MB. Then the UV-vis absorption of the MB solution was measured at 0, 6, and 12 h.

2.6. In vitro intracellular uptake study

To evaluate the uptake of Met–GOx/Fe@LE NPs and their cellular distribution pattern, rhodamine B-modified GOx (RhBGOx) was synthesized according to a previous study [35] and Met–RhBGOx/Fe@LE NPs were prepared as described above. 4T1 cells were seeded in 48-well plates at a density of 1×10^4 cells/well for 24 h. After incubation with RhBGOx and Met–RhBGOx/Fe@LE NPs for 0.5, 2, and 4 h, the treated cells were washed with PBS (pH 7.4) three times, fixed with 4% paraformaldehyde for 30 min, stained with DAPI for 5 min, and finally observed with an ApoTome.2 (Zeiss, Baden-Wurttemberg, Germany). Flow cytometry (NovoCyte, San Diego, CA, USA) was further used to investigate cell uptake.

2.7. Monitoring the intracellular glucose and ATP levels

For intracellular glucose level assessment, 4T1 cells were cultured and incubated with different formulations for 12 h, using fresh medium as a control. After incubation, amount of cellular glucose was measured following the procedures provided by the Glucose Assay Kit from Beyotime Biotechnology (Cat# S0201S).

To estimate the intracellular ATP level, 4T1 cells cultured in 96-well plates were collected, lysed, and centrifuged at 12,000 *g* for 5 min. Then, the intracellular ATP content in each group was measured with a standard ATP Luminescent Cell Viability Assay Kit (Cat# 40210ES10; Yeasen Biotechnology Co., Ltd., Shanghai, China) and a microplate reader.

2.8. Cell proliferation and cytotoxicity assays in vitro

An EdU detection kit (Cat# C10071S; BeyoClick™ EdU-488, Beyotime Biotechnology) was employed to study tumor cell proliferation after different treatments with the help of fluorescence microscopy observations and flow cytometry. Briefly, 4T1 cells were seeded in 24-well plates (2.0×10^4 per well) for 24 h. The incubation media were then replaced with fresh media containing Fe@LE NPs, Met, GOx, Met/Fe@LE NPs, GOx/Fe@LE NPs, or Met–GOx/Fe@LE NPs, using fresh medium as a control. Each sample had a fixed GOx concentration equivalent to 20 mU/mL. After incubation for another 4 h, EdU working solution was added for another 2 h of incubation. After that, the cells were fixed with 4% (*V*/*V*) paraformaldehyde, permeabilized with 0.3% Triton-100, incubated with EdU reaction solution, and stained with Hoechst 33342. The stained cells were observed with an Olympus inverted fluorescence microscope (Olympus TH4-200; Tokyo, Japan).

The intracellular pH of 4T1 cells was determined after incubation with different formulations for 4 h and analyzed with the pH-sensitive probe pHrodo™ Green AM. Furthermore, mitochondrial damage in 4T1 cells treated with different formulations was evaluated by examining the mitochondrial membrane potential by JC-1 staining. Reactive oxygen species (ROS) production in 4T1 cells was detected by staining with 2',7'-dichlorofluorescin diacetate (DCFH-DA, Cat# D6883; Sigma-Aldrich) according to previous studies [36,37]. To further evaluate the cytotoxicity of different formulations, a live/dead assay was performed to observe the cell killing effect using calcein-AM/PI (Cat# MA0361; Dalian Meilun Biotechnology Co., Ltd.).

2.9. Cell apoptosis assay

The toxicity of Met–GOx/Fe@LE NPs to 4T1 cells was evaluated by an annexin V-FITC/7AAD Kit. After incubation in 6-well plates for 24 h, Fe@LE NPs, Met, GOx, Met/Fe@LE NPs, GOx/Fe@LE NPs, and Met–GOx/Fe@LE NPs were added to the cells for 24 h of incubation. Then, the 4T1 cells were collected, and cell apoptosis was recorded by flow cytometry (ACEA NovoCyte).

2.10. In vivo biodistribution and imaging

Female BALB/c mice (6 weeks old, 18–20 g) were purchased from the Animal Center Laboratory of Beijing HFK Bioscience Co., Ltd. (Beijing, China). All animal procedures strictly complied with the Guidelines for Care and Use of Laboratory Animals of Sichuan University and were approved by the Animal Ethics Committee of West China Hospital of Sichuan University (IACUC No: 202221028003). The tumor-bearing mouse model was established by injecting 5×10^5 4T1 cells (in 50 μL of culture medium) into the fat pad of the right fourth breast according to our previous studies [34,38].

To determine the biodistribution of the nanocarriers, tumor-bearing mice were treated with RhBGOx and Met–RhBGOx/Fe@LE NPs. At predetermined time intervals (2, 4, 8, 12, and 24 h), fluorescence images of the 4T1 model mice were acquired with the IVIS Lumina series III system (PerkinElmer, Waltham, MA, USA). *Ex vivo* fluorescence images were then taken 24 h after intravenous injection. The tumor nodules were sliced and stained with a rabbit monoclonal antibody against CD31 (Cat# ab222783; Abcam, Shanghai, China) to further observe the distribution of the Met–RhBGOx/Fe@LE NPs.

2.11. Antitumor effects in vivo

Breast tumor-bearing mice were intravenously injected with 100 μL of normal saline, Fe@LE NPs, Met, GOx, Met + GOx, Met/Fe@LE NPs, GOx/Fe@LE NPs, or Met–GOx/Fe@LE NPs, with fixed GOx concentration equivalent to 2 mg/kg body weight. Tumor volume and mouse body weight were recorded every 3 for 15 days. On the last day, all mice were euthanized, and the tissues were collected, fixed, embedded, and stained according to typical hematoxylin-eosin (H&E) staining protocols. The intertumoral levels of ATP after various treatments were measured by an ATP Luminescent Cell Viability Assay Kit (Cat# 40210ES10; Yeasen Biotechnology Co., Ltd.) according to a previous study [4]. In brief, the tumors were harvested, digested by collagenase IV, hyaluronidase, and deoxyribonuclease and then filtered through 75-mm filters to obtain monodispersed tumor cells. The monodispersed tumor cells were collected, lysed, and centrifuged at 12,000 *g* for 5 min. Then, the intracellular ATP content in each group was measured. Moreover, the ROS level was evaluated by dihydroethidium (DHE) staining of tumor tissue sections according to a previous study [12].

In addition, the tumors were stained with anti-Ki67 (Cat# ab15580, rabbit; Abcam), anti-caspase 9 (Cat# ab202068, rabbit; Abcam), and anti-cleaved caspase 9 (Cat# YC0014, rabbit; Immunoway, Suzhou, China) followed by treatment with HRP-conjugated goat anti-rabbit IgG heavy and light chains (Cat# ab672; Abcam). Terminal deoxynucleotidyl transferase dUTP nick end labeling (TUNEL) was carried out to assess histological damage using an *in situ* cell death detection kit (Cat# 11684817910; Roche, Shanghai, China).

2.12. Statistical analysis

All statistical analyses were performed using Prism software (GraphPad Software, La Jolla, CA, USA). All the data are presented as the mean ± standard deviation (SD) unless stated otherwise. Error bars represent the standard deviation of the mean from independent samples studied. We assumed a normal distribution of data. Student's *t*-test was applied to detect significant differences between two experimental groups (with $P < 0.05$).

3. Results and discussion

3.1. Characterization of the LE conjugate

CS is a widely used cationic copolymer with excellent biocompatibility, biodegradability, and drug loading ability [15,39]. However, its limited water solubility hinders its application in the field of biomedicine. Fortunately, the abundant amino groups on the CS skeleton make its modification through cross-linking reactions easy. Increasingly, studies have shown that the major catechin component EGCG can interact with various materials (such as proteins, peptides, nucleic acids, and metal ions) and induce apoptosis in cancerous cells [24]. LC was modified with EGCG to synthesize the LE conjugate. As shown in Fig. S1A, the LE conjugate was light yellow and had good water solubility. The visible peak at approximately 7.0 ppm in the LE spectrum (Fig. S1B) is characteristic of EGCG, proving the successful conjugation, which was consistent with a previous study [30]. The FTIR spectra of LC, EGCG and the LE conjugate are shown in Fig. S1C. The formation of the new peaks at 1638.10, 1562.17, and 1412.38 cm^{-1} observed in the

spectrum of the LE conjugate was attributed to C=C stretching vibrations. As depicted in Fig. S1D, the UV-vis spectrum of the LE conjugate showed a typical peak at 273 nm, which is attributed to the π–π* transition of the phenolic group in EGCG, indicating the successful insertion of EGCG into CS.

3.2. Characterization of the Met–GOx/Fe@LE NPs

Multiple studies have reported that Met not only can be used for diabetes treatment but also can serve as a unique agent for neuroprotection, cardiovascular protection, and cancer therapy [6,40]. GOx, an enzyme that catalyzes the conversion of glucose to gluconolactone, can synergize with therapeutic agents to enhance their anticancer efficacy while depleting the local glucose concentration [41,42]. We hypothesized that Met and GOx could confer enhanced antiproliferative efficacy via metabolism disruption and glucose starvation synergistic therapy. It would be clinically significant to develop a new nanoplatform to enhance the delivery efficacy of Met/GOx to tumor cells. A schematic illustration of the Met–GOx/Fe@LE NPs preparation process is displayed in Fig. 2A.

To optimize the final concentration of LE and Fe^{3+}, a series of Fe@LE NPs were prepared and their size was measured using DLS (Fig. S2). As shown, the hydrodynamic diameter of the Fe@LE NPs could be readily tuned in the range of 180 and 1020 nm by simply adjusting the feeding ratios of LE and Fe^{3+}. Considering the particle size of Fe@LE NPs and the Fenton reaction induced by Fe^{3+} in the acidic tumor microenvironment, 20 mM $FeCl_3$ was selected as the optimal concentration. As the next influencing parameter, the effect of the sonication time on the particle size of the different nanoparticles was studied in the range of 10–120 s. As displayed in Fig. S3, increasing the sonication time decreased the particle size, and no significant changes were observed after 60 s. Hence, a sonication time of 60 s was chosen as the optimum sonication time for further investigation. The concentration of Fe^{3+} (20 mM) and the sonication time (60 s) were then fixed, and the stability of these nanoparticles was determined using DLS. All of the Fe@LE NPs, Met/Fe@LE NPs, GOx/Fe@LE NPs, and Met–GOx/Fe@LE NPs showed great stability in PBS (pH 7.4) (Fig. S4).

According to the TEM images (Fig. 2B) and particle size distribution (Fig. 2C) of the Fe@LE NPs, Met/Fe@LE NPs, GOx/Fe@LE NPs, and Met–GOx/Fe@LE NPs, the obtained nanocarriers were spherical in shape with an average hydrated diameter of approximately 190 nm. The sizes of these nanocarriers as measured by DLS were larger than those measured by TEM because of the hydrated polymer coating on the former samples [15]. To evaluate the successful loading of GOx into Met–GOx/Fe@LE NPs, SDS-PAGE was applied. As shown in Fig. S5, Met–GOx/Fe@LE NPs appeared as a very weak band in the 10% SDS-PAGE gel, while GOx migrated and appeared as a single broad band in the gel, which may be a result of the successful loading of GOx in Met–GOx/Fe@LE NPs [43,44]. A GOx DL content of 15.0% and drug EE of 93.0% were obtained, while Met documented a DL and EE of 14.3% and 88.0%, respectively.

To further study the mechanism of the Fe@LE NPs loaded with GOx and Met, the independent gradient model based on the Hirshfeld partition method was introduced via the Multiwfn program, with an isosurface visualized by the visual molecular dynamics (VMD) program [45–47]. As shown in Fig. S6, the blue, red, and green isosurface regions indicate the attractive (hydrogen bonding or electrostatic attractions), repulsive (such as steric effects), and van der Waals interactions, respectively. The interaction energy between Fe@LE NPs and GOx (−49.094 kcal/mol) was higher than the interaction energy between Fe@LE NPs and Met (−30.071 kcal/mol), and there was a high interaction energy between Fe@LE NPs and GOx-Met (−79.742 kcal/mol). This strong interaction contributed to the high drug loading and stability of the Met–GOx/Fe@LE nanoplatform [48].

The corresponding TEM-energy dispersive spectroscopy (TEM-EDS) mapping results of the Met–GOx/Fe@LE NPs (Fig. 2D) showed evident carbon, nitrogen, oxygen, and iron signals. The FTIR spectrum (Fig. S7A) showed broad bands at 3189 and 3371 cm^{-1} that were attributed to the O–H stretching and N–H stretching modes of Met [49]. The characteristic peaks of the amide group at 1641 and 1559 cm^{-1} were attributed to the C=O vibration and N–H bending vibration of GOx [9]. In the FTIR spectrum of Met–GOx/Fe@LE NPs, the peaks at 3180, 937, and 741 cm^{-1} were attributed to Met and the additional peak at 1638 cm^{-1} was ascribed to GOx, which was indicative of successful drug loading. Furthermore, as shown in Fig. S7B, the characteristic peaks of the Met–GOx/Fe@LE NPs were located at 12.1°, 17.3°, 22.4°, 23.1°, 24.3°, 28.7°, and 31.5°, which correspond to the characteristic peaks of Met at 12.44°, 17.8°, 22.4°, 23.3°, 24.4°, 28.1°, 31.1°, and 37.1°, respectively [50]. All the above results were indicative of successful drug loading.

3.3. Drug release, catalytic ability, and enzymatic activity analyses

The drug release behavior from the Met–GOx/Fe@LE NPs was determined by immersing the nanocarriers in PBS at different pH values (7.4, 6.8, and 5.4) according to previous studies [4,11]. As depicted in Figs. 3A and B, the loaded GOx and Met was released in a pH dependent manner. Notably, the amount of GOx released from the Met–GOx/Fe@LE NPs was 64.7% (pH 5.4), 30.4% (pH 6.8), and 24.3% (pH 7.4), and the amount of Met released was 60.8% (pH 5.4), 27.7% (pH 6.8), and 22.3% (pH 7.4) after 12 h of incubation. It is reasonable to assume that with the decrease in pH from 7.4 to 5.4, the amine groups of CS become protonated and the coordination between EGCG and Fe^{3+} can be broken, resulting in the structural disintegration and degradation of the Met–GOx/Fe@LE NPs [15]. To further verify the pH responsiveness, the biodegradation of the Met–GOx/Fe@LE NPs in different environments (pH 7.4, 6.8, and 5.4) was directly observed by TEM (Fig. 3C). The microstructure of the Met–GOx/Fe@LE NPs did not obviously change under neutral conditions (pH 7.4), suggesting that the Met–GOx/Fe@LE NPs may maintain their integrity in blood circulation. After infiltration for 12 h in mildly acidic solution (pH 6.8), the Met–GOx/Fe@LE NPs gradually disintegrated, while the nanoplatform was completely degraded after immersion in acidic PBS (pH 5.4) for 12 h.

GOx catalyzes the decomposition of glucose, O_2, and H_2O to produce H_2O_2 and gluconic acid, resulting in tumor cell starvation to improve the efficacy of combination therapy [51,52]. For the catalytic activity assay, GOx, GOx/Fe@LE NPs, and Met–GOx/Fe@LE NPs were added to a working solution containing HRP/dianisidine/glucose. GOx alone and GOx in the GOx/Fe@LE NPs and Met–GOx/Fe@LE NPs could catalyze the reaction of glucose to produce H_2O_2, which could be further catalyzed by HRP to generate ·OH. The concentration of H_2O_2 notably increased with increasing glucose concentration, and the content of H_2O_2 in the GOx/Fe@LE NPs and Met–GOx/Fe@LE NPs groups slightly decreased compared to that in the GOx group (Fig. 3D), suggesting that these nanocarriers can retain the catalytic activity of GOx.

The multivalent metal ion pair Fe^{2+}/Fe^{3+} is an available Fenton agent that can catalyze the decomposition of H_2O_2 into highly cytotoxic ·OH, thus triggering chemodynamic therapy to induce apoptosis or necrosis [53–55]. However, insufficient level of endogenous H_2O_2 and ·OH scavenged by glutathione that is overexpressed in cells result in unsatisfactory antitumor efficiency [54]. Phenols such as EGCG, tannic acid, and gallic acid have been proven to reduce Fe^{3+} into Fe^{2+} to participate in efficient Fenton reactions

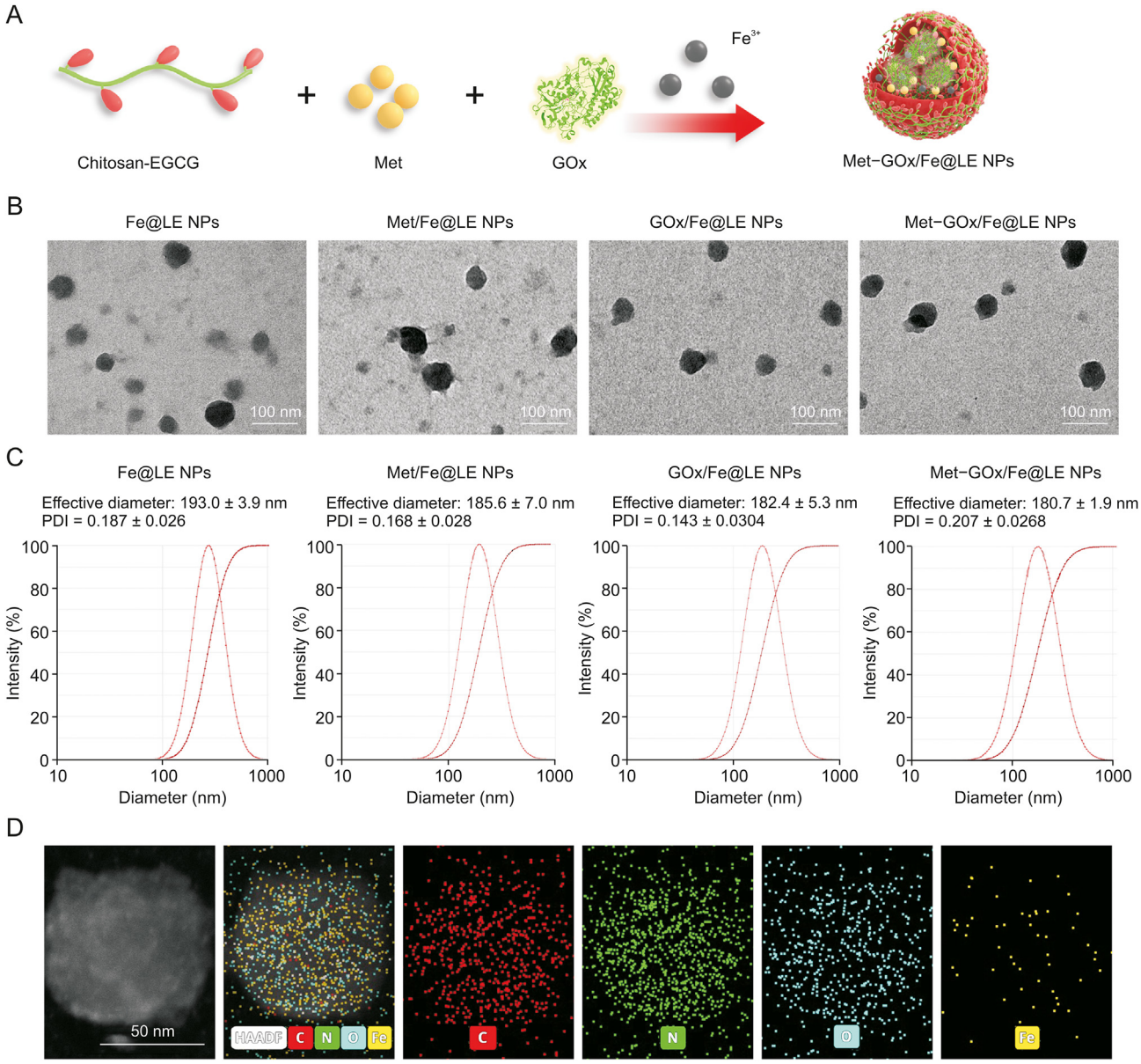

Fig. 2. Characterization of metformin (Met)–glucose oxidase (GOx)/Fe@epigallocatechin gallate (EGCG)-conjugated low-molecular-weight chitosan (LC-EGCG, LE) nanoparticles (NPs). (A) Schematic illustration of the preparation process of Met–GOx/Fe@LE NPs. (B, C) Transmission electron microscopy (TEM) images (B) and particle size distribution (C) of Fe@LE NPs, Met/Fe@LE NPs, GOx/Fe@LE NPs, and Met–GOx/Fe@LE NPs. (D) The corresponding energy-dispersive spectroscopy (EDS) results of Met–GOx/Fe@LE NPs. PDI: polydispersity index; HAADF: high-angle annular dark-field.

[33,34]. Based on this, we assume that the pH-triggered Met–GOx/Fe@LE NPs can be degraded under acidic conditions, and the released GOx can effectively catalyze glucose to produce H_2O_2, and the GOx-catalyzed H_2O_2 can be further decomposed into ·OH based on the subsequent Fenton reaction. As shown in Fig. S8, ·OH generation was detected by the degradation of MB after treatment with GOx, Fe@LE NPs, GOx/Fe@LE NPs, and Met–GOx/Fe@LE NPs. In the presence of GOx and with a decrease in the pH from 7.4 to 5.4, a gradual decrease in MB absorption was noted in the GOx/Fe@LE NPs and Met–GOx/Fe@LE NPs groups (Fig. S8), further suggesting pH responsiveness. No obvious decrease in MB absorption was observed in the Fe@LE NPs group, probably because H_2O_2 was not produced. It is noteworthy that limited ·OH signals were observed in the GOx alone group, suggesting that the absence of the Fenton reaction restricts the continuous generation of ·OH.

Consistent with a previous study, the enzymatic activities of GOx, GOx/Fe@LE NPs, and Met–GOx/Fe@LE NPs (Fig. 3E) were then determined. GOx/Fe@LE NPs and Met–GOx/Fe@LE NPs retained approximately 73% of their initial enzyme activity after storage at 37 °C for seven days, whereas the enzyme activity of GOx alone was quickly lost and only 20.5% was retained under the same storage conditions [11]. It has been well established that pH has a large effect on the catalytic activity of GOx [56]. As expected, acid/base (pH 4.0/pH 10.0) treatments significantly decreased the catalytic activity decrease of free GOx, while Met–GOx/Fe@LE NPs retained much higher activity (Fig. S9). Notably, Met–GOx/Fe@LE NPs maintained almost all of their catalytic activity in tumor endosomal (pH 5.5)/weakly acidic tumor (pH 6.5) microenvironments [57]. All these results suggested that Met–GOx/Fe@LE NPs can retain the enzyme activity of GOx while improving its stability.

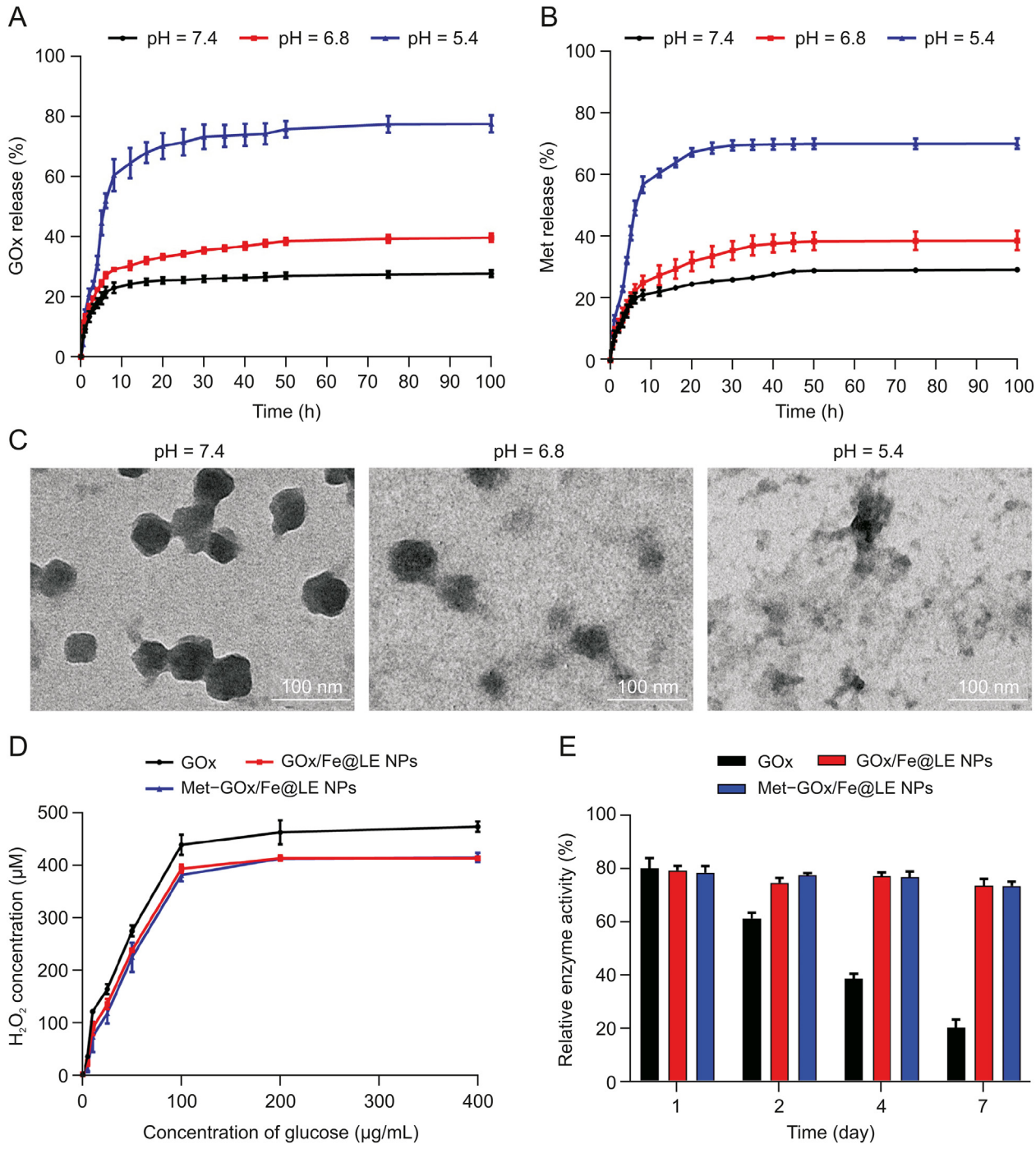

Fig. 3. Release profile and catalytic capability of metformin (Met)–glucose oxidase (GOx)/Fe@epigallocatechin gallate (EGCG)-conjugated low-molecular-weight chitosan (LC-EGCG, LE) nanoparticles (NPs). (A, B) Relative amount of GOx (A) and Met (B) released from Met–GOx/Fe@LE NPs in phosphate-buffered saline (PBS) under different pH conditions ($n = 3$). (C) Degradation of Met–GOx/Fe@LE NPs at different pH values after 12 h. (D) The concentration of generated H_2O_2 at different glucose concentrations due to the Met–GOx/Fe@LE NPs-catalyzed oxidation of glucose. (E) Enzymatic activity of GOx, GOx/Fe@LE NPs, and Met–GOx/Fe@LE NPs at 37 °C (GOx: 1.0 μg/mL, $n = 6$).

3.4. Cellular uptake study

To assess the specific internalization of Met–GOx/Fe@LE NPs, RhBGOx was used as a fluorescent probe. Compared to that in the RhBGOx-treated group, brighter red fluorescence was detected in 4T1 cells incubated with Met–RhBGOx/Fe@LE NPs for 0.5, 2, and 4 h (Fig. 4A). Flow cytometry (Fig. 4B) and the corresponding quantitative analysis (Fig. 4C) were performed to further measure the fluorescence intensity. As shown, the fluorescence intensity in the Met–GOx/Fe@LE NPs-treated group was significantly stronger than that in the RhBGOx-treated group at every time point. This phenomenon is mainly due to endocytosis of the nanocarriers, whereas the native protein RhBGOx cannot readily permeate the cell membrane [58].

3.5. Intracellular glucose and ATP level analyses

To determine the glucose abundance in 4T1 cells after different treatments, the intracellular glucose levels were measured. Compared to the control group, Fe@LE NPs-, Met-, and Met/Fe@LE

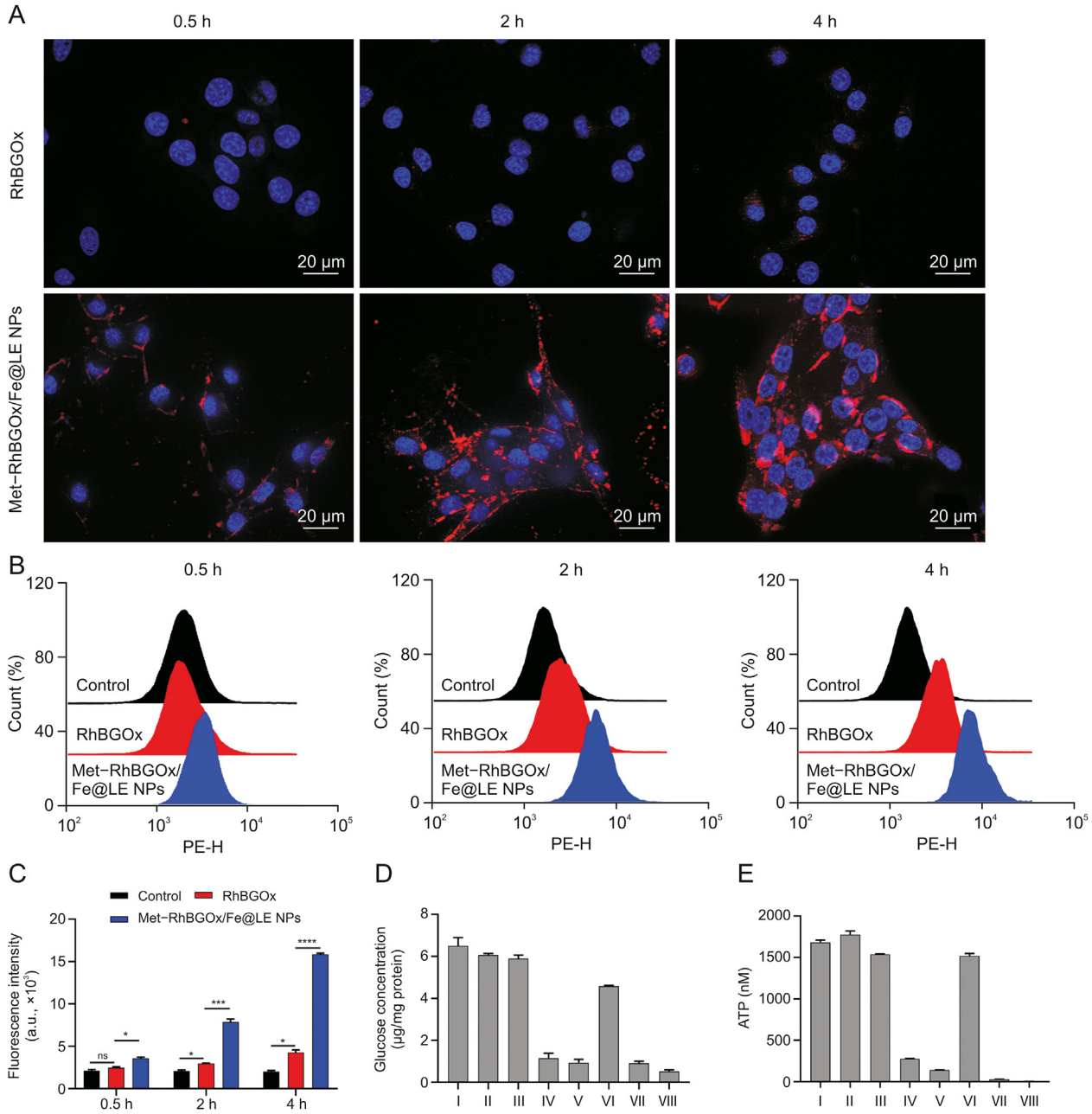

Fig. 4. *In vitro* intracellular uptake study. (A, B) Confocal laser scanning microscopy (CLSM) images (A) and flow cytometry analysis (B) of 4T1 cells after exposure to rhodamine B-modified glucose oxidase (RhBGOx) and metformin (Met)–RhBGOx/Fe@epigallocatechin gallate (EGCG)-conjugated low-molecular-weight chitosan (LC-EGCG, LE) nanoparticles (NPs) (RhBGOx concentration: 10 μg/mL) for 0.5, 2, and 4 h. (C) Quantitative results of cell uptake. (D) Changes in glucose abundance in 4T1 cells after incubation with different groups. (E) Changes in the adenosine triphosphate (ATP) levels of 4T1 cells after various treatments for 24 h ($n = 6$). I: control; II: Fe@LE NPs; III: Met; IV: GOx; V: Met + GOx; VI: Met/Fe@LE NPs; VII: GOx/Fe@LE NPs; and VIII: Met–GOx/Fe@LE NPs. $^{*}P < 0.05$, $^{***}P < 0.001$, and $^{****}P < 0.0001$; ns: no significance. PE: P-phycoerythrin.

NPs-treated cells failed to show substantial changes in glucose levels, while GOx-, Met + GOx-, Met/Fe@LE NPs-, GOx/Fe@LE NPs-, and Met–GOx/Fe@LE NPs-treated cells displayed significant decreases in intracellular glucose levels (Fig. 4D), which was directly due to GOx-mediated glucose depletion [11]. Previous studies have proven that glycolysis inhibition by GOx-loaded nanosystems could significantly reduce ATP production [59,60]. Moreover, the ATP production assay results (Fig. 4E) indicated that GOx, Met + GOx, Met/Fe@LE NPs, GOx/Fe@LE NPs, and Met–GOx/Fe@LE NPs could induce a significant decrease in ATP levels.

3.6. Cell proliferation and cytotoxicity assays in vitro

The efficacy of metabolism disruption and glucose starvation synergistic therapy was examined by using a BeyoClick™ EdU-488 assay kit (Fig. 5A) and calcein-AM/PI double staining (Fig. 5B). Cells treated with Met–GOx/Fe@LE NPs showed sparse green EdU fluorescence and the most intense red fluorescence (dead cells) among the groups, demonstrating that the nanocarriers efficiently inhibited 4T1 cells. GOx-based nanocarriers can mediate a significant decrease in intracellular pH and an increase in ROS levels [61]. Unsurprisingly, Met–GOx/Fe@LE NPs significantly increased the

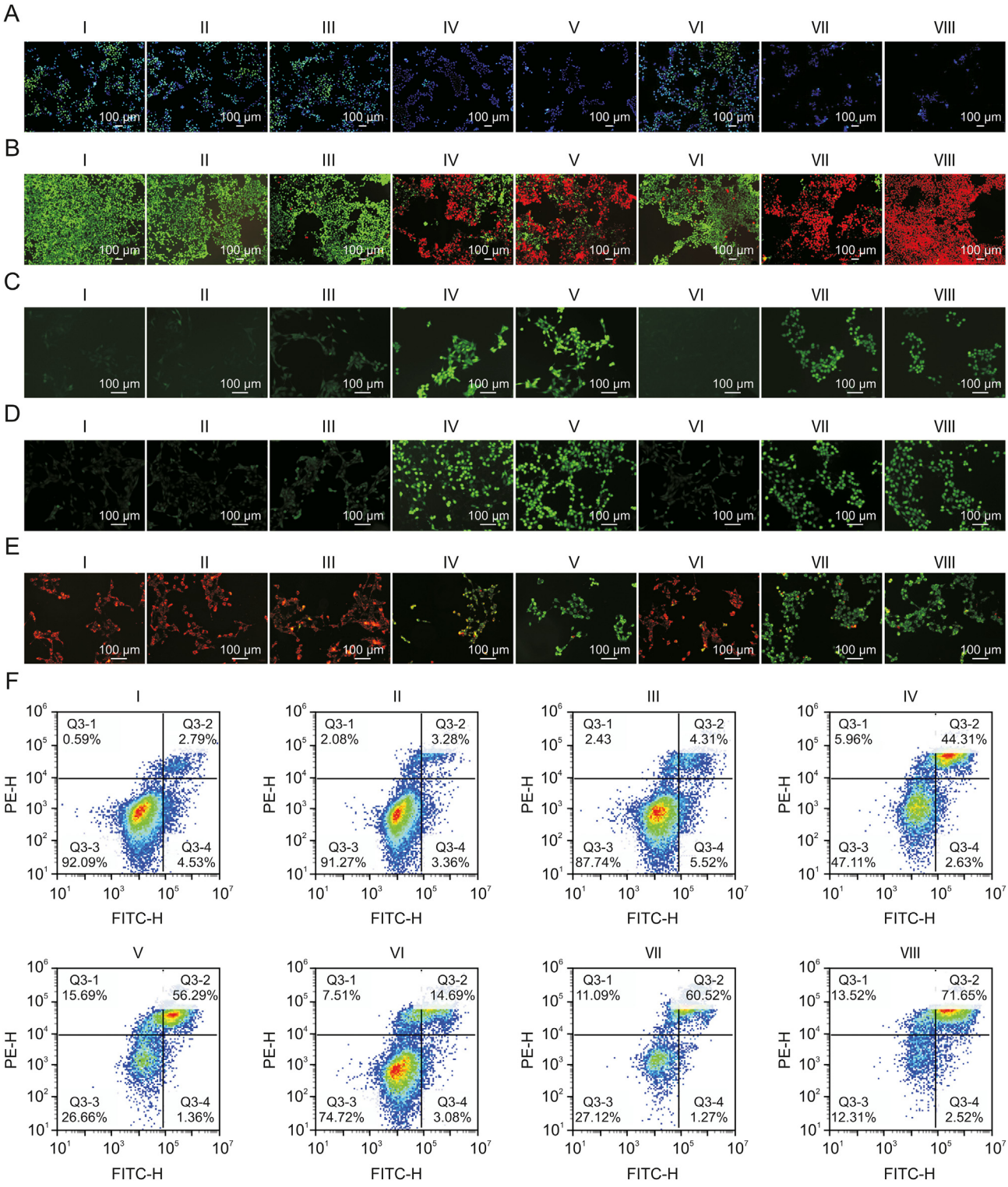

Fig. 5. The cell proliferation and apoptotic assays *in vitro* treated with metformin (Met)–glucose oxidase (GOx)/Fe@epigallocatechin gallate (EGCG)-conjugated low-molecular-weight chitosan (LC-EGCG, LE) nanoparticles (NPs). (A) Confocal laser scanning microscopy (CLSM) observation on the proliferation levels of 4T1 cells after incubation with different groups, probed by BeyoClick™ EdU-488. (B) Calcein-acetoxymethyl ester (AM)/propidium iodide (PI) double stain of 4T1 cells treated with different formulations. (C) The reactive oxygen species (ROS) levels in 4T1 cells after incubation for 4 h and stained with 2,7-dichlorodihydrofluorescein diacetate (DCFH-DA). (D) CLSM observation on the intracellular pH of 4T1 cells after incubation with different groups for 4 h, probed by pH-sensitive pHrodo™ Green AM probe. (E) The changes in the mitochondrial membrane potential of 4T1 cells after different treatment for 4 h. (F) The cell apoptotic analyses of 4T1 cells treated with different formulations for 24 h. I: control; II: Fe@LE NPs; III: Met; IV: GOx; V: Met + GOx; VI: Met/Fe@LE NPs; VII: GOx/Fe@LE NPs; and VIII: Met–GOx/Fe@LE NPs. PE: P-phycoerythrin; FITC: fluorescein isothiocyanate.

ROS levels (Fig. 5C) and decreased the pH (Fig. 5D) in 4T1 cells, proving that the GOx released from the GOx/Fe@LE NPs and Met–GOx/Fe@LE NPs effectively starved tumor cells by depleting the glucose supply. However, Met–GOx/Fe@LE NPs produced a slight decrease in ROS levels and a slight increase in intracellular pH compared with free GOx and GOx/Fe@LE NPs due to the inhibition

of glycolysis by Met [62,63]. After JC-1 staining (Fig. 5E), the mitochondria in the Fe@LE NPs, Met and Met/Fe@LE NPs groups remained normal, as indicated by the J-aggregates that emitted red fluorescence, whereas the mitochondria in the GOx, GOx + Met, GOx/Fe@LE NPs, and Met–GOx/Fe@LE NPs groups exhibited varying degrees of damaged mitochondria, as indicated by the monomers that emitted green fluorescence [51,59].

To investigate the therapeutic efficacy of Met–GOx/Fe@LE NPs in 4T1 cells, we assessed their apoptotic effect by flow cytometry (Fig. 5F). As expected, treatment with Met–GOx/Fe@LE NPs led to the greatest ratio of dead/apoptotic cells among the groups (approximately 74.1%), which was higher than those produced in the GOx/Fe@LE NPs (61.8%), GOx + Met (57.9%), and GOx alone (46.9%) groups, and these results were consistent with those from live/dead staining. Met and Met/Fe@LE NPs induced slight dead/apoptosis (9.8% and 17.8%, respectively). Slight dead/apoptosis was observed in the control group (7.3%) because of the aggressive growth and rapid metabolism in these cells, which has been reported previously in the literature [64]. This was expected since the additional Met in GOx + Met and the Met–GOx/Fe@LE NPs can decrease ATP production and tumor cell O_2 consumption [12,44].

3.7. In vivo biodistribution

The enhanced tumor penetration of therapeutic agents mediated by nanoparticle-based approaches is key to improving anticancer efficacy [58]. The positively charged amino groups of CS can interact with the negatively charged biological membranes to enhance the endocytosis of CS-based nanocarriers [19]. In this study, the *in vivo* biodistribution of Met–RhBGOx/Fe@LE NPs was examined in 4T1 tumor-bearing BALB/c mice by live imaging. Eight hours after i.v. injection, only a small amount of free RhBGOx was observed in the tumors (Fig. 6A), probably due to the highly restrictive transcytosis of proteins [58]. In contrast, more nanoparticles accumulated in the tumor site, as evidenced by the stronger fluorescence intensity in these tumors than that in the free RhBGOx group, which may be attributed to the enhanced intratumoral diffusion of the RhBGOx released from Met–RhBGOx/Fe@LE NPs. After staining with CD31 to locate the blood vessels, the penetration and intratumoral diffusion of Met–RhBGOx/Fe@LE NPs were further assessed. Consistent with the *in vivo* imaging data, stronger fluorescence signals were observed in the Met–RhBGOx/Fe@LE NPs groups than in the free RhBGOx group (Fig. 6B). Likewise, quantitative analysis of the distribution in the major organs indicated that the intracranial accumulation of Met–RhBGOx/Fe@LE NPs was 3.6-fold higher than that of free RhBGOx (Figs. 6C and D). Moreover, the fluorescence intensities in the hearts, livers, spleens, lungs, and kidneys in all groups were not significantly different.

3.8. In vivo anticancer effect

Encouraged by the superior intratumoral diffusion of the Met–RhBGOx/Fe@LE NPs, the therapeutic effect of these

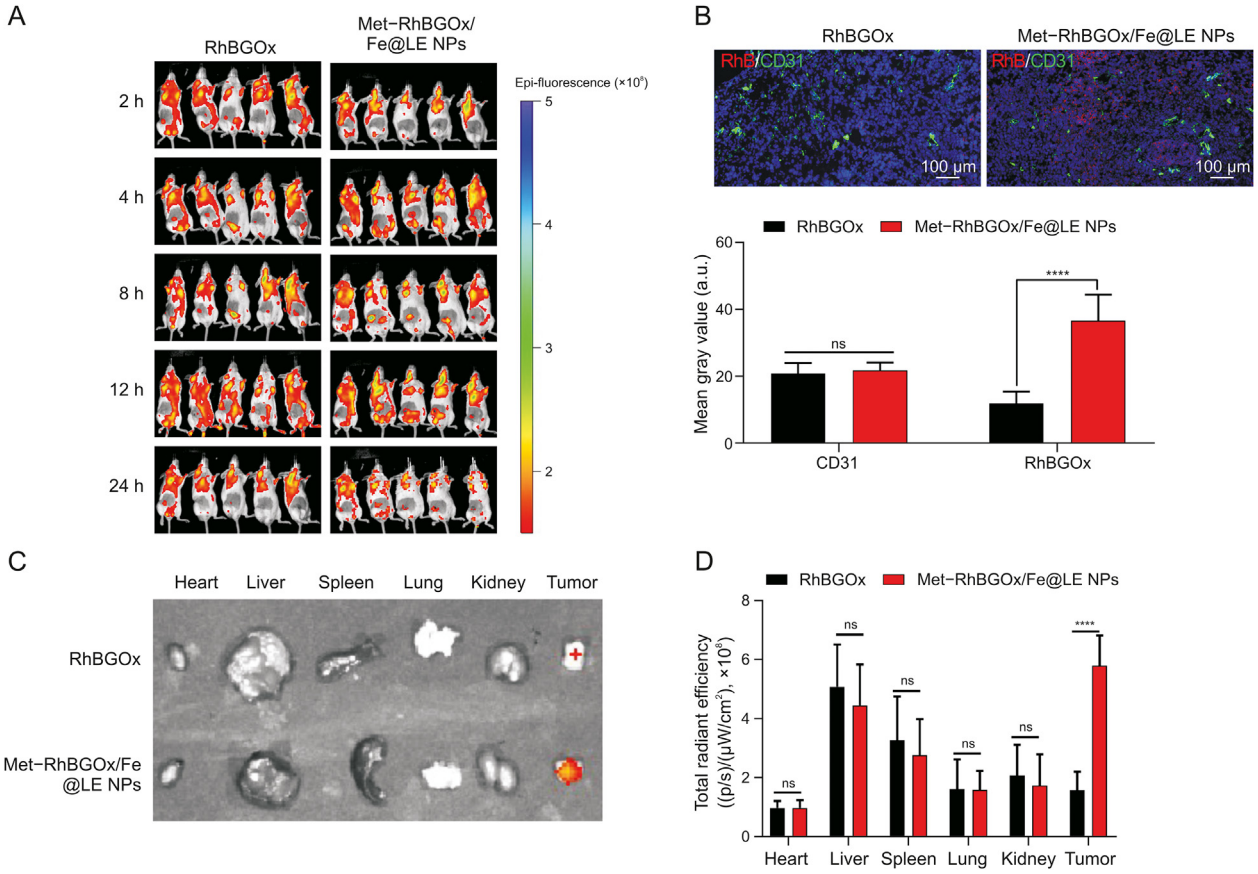

Fig. 6. Biodistribution of metformin (Met)–rhodamine B-modified glucose oxidase (RhBGOx)/Fe@epigallocatechin gallate (EGCG)-conjugated low-molecular-weight chitosan (LC-EGCG, LE) nanoparticles (NPs) in tumor-bearing mice. (A) The fluorescence images were collected at 1, 2, 4, 8, 12, and 24 h after intravenous injection in 4T1 model. (B) Distribution of RhBGOx in tumors with various treatments; CD31 was stained with anti-CD31-fluorescein isothiocyanate (FITC) antibody. Semi-quantitative analysis of CD31 and RhBGOx was performed using the ImageJ software. (C) The *ex vivo* fluorescence imaging of heart, liver, spleen, lung, kidney, and tumor collected at 24 h after intravenous injection. (D) Quantification of RhBGOx distribution in the major organs at 24 h after injection. $^{***}P < 0.001$ and $^{****}P < 0.0001$; ns: no significance.

nanoparticles on 4T1 tumor-bearing BALB/c mice was evaluated. The mice were intravenously injected with normal saline (control), Fe@LE NPs, Met, GOx, Met + GOx, Met/Fe@LE NPs, GOx/Fe@LE NPs, or Met–GOx/Fe@LE NPs. According to the tumor growth curves in Fig. 7A, the Met–GOx/Fe@LE NPs-treated group exhibited significant tumor inhibition compared with the GOx/Fe@LE NPs group ($P < 0.05$), Met/Fe@LE NPs group ($P < 0.01$), Met + GOx group ($P < 0.01$), GOx group ($P < 0.01$), Met group ($P < 0.001$), Fe@LE NPs ($P < 0.001$), and normal saline group ($P < 0.0001$). The stronger anticancer effect of Met–GOx/Fe@LE NPs was probably caused by the released GOx that can deplete the Met-induced accumulation of intracellular glucose and induce glucose starvation. The relatively weak therapeutic effects observed in the Met, GOx, and Met + GOx groups may be due to ineffective tumor accumulation [4]. After treatment, the tumors were collected and analyzed (Figs. 7B and C). As shown, the measured tumor weights and digital photos of animals in the Met–GOx/Fe@LE NPs group also suggest that these nanoparticles have a better tumor inhibition effect, which is consistent with the above results.

The H&E staining images of the tumor sections (Fig. 7D) showed noticeable cell death in the Met–GOx/Fe@LE NPs and GOx/Fe@LE NPs groups, while no obvious cell death was found in the Met, GOx, Met + GOx, or Met/Fe@LE NPs groups compared to the normal saline group. As shown in Fig. S10, there was no apparent histological damage to the heart, spleen, lung, or kidney after treatment with different formulations. Clear liver metastases (Fig. 7E) were found in the normal saline (control), Fe@LE NPs, Met, and GOx groups, with a slight decrease in liver metastases in the Met + GOx and Met/Fe@LE NPs groups. Liver metastases were significantly inhibited by Met–GOx/Fe@LE NPs, further proving the superior antitumor efficacy of this nanoplatform.

To elucidate the *in vivo* anticancer mechanism, TUNEL immunofluorescence, Ki67, and cleaved caspase 9 immunohistochemical staining of tumor slices were performed according to our previous studies [14]. The results shown in Figs. 8A–D suggested that the Met–GOx/Fe@LE NPs induced more tumor cell apoptosis/death and lower rates of proliferation. According to the TUNEL results (Figs. 8A and S11A), the apoptotic index in the Met–GOx/Fe@LE NPs-treated group was 80.0% ± 8.7% compared with those in the GOx/Fe@LE NPs group (68.2% ± 8.4%, $P < 0.05$), Met/Fe@LE NPs group (48.2% ± 7.8%, $P < 0.0001$), Met + GOx group (43.2% ± 9.8%, $P < 0.0001$), GOx group (27.8% ± 3.9%, $P < 0.0001$), Met group (21.8% ± 4.9%, $P < 0.0001$), Fe@LE NPs group (16.2% ± 3.5%, $P < 0.0001$), and normal saline group (8.4% ± 3.8%, $P < 0.0001$). There was no significant difference between the normal saline-, Fe@LE NPs-, and Met-treated groups ($P > 0.05$). The Ki-67 LI was also analyzed (Fig. S11B), the Met–GOx/Fe@LE NPs-treated group had a lower Ki67-LI (8.2% ± 2.2%) than the GOx/Fe@LE NPs group (21.6% ± 5.7%, $P < 0.05$), Met/Fe@LE NPs group (50.0% ± 8.7%, $P < 0.0001$), Met + GOx group (50.6% ± 6.3%, $P < 0.0001$), GOx group (71.8% ± 6.0%, $P < 0.0001$), Met group (69.0% ± 7.3%, $P < 0.0001$), Fe@LE NPs group (77.6% ± 8.7%, $P < 0.0001$), and normal saline group (77.2% ± 11.1%, $P < 0.0001$). Notably, the Ki67-LI was not significantly different between the normal saline-, Fe@LE NPs-, Met-, and GOx-treated groups ($P > 0.05$).

AKT activation has been shown to enhance glycolysis and promote cancer growth; thus, inhibiting its activation may enhance anticancer effects [62]. Met effectively restrains the glycolytic phenotype of tumor cells and causes a reduction in glycolysis [5,7]. Western blot analysis of p-AKT after different treatments (Fig. 8E) suggested that Met + GOx, GOx/Fe@LE NPs, and Met–GOx/Fe@LE NPs can notably decrease the activation of AKT (p-AKT). Met–GOx/

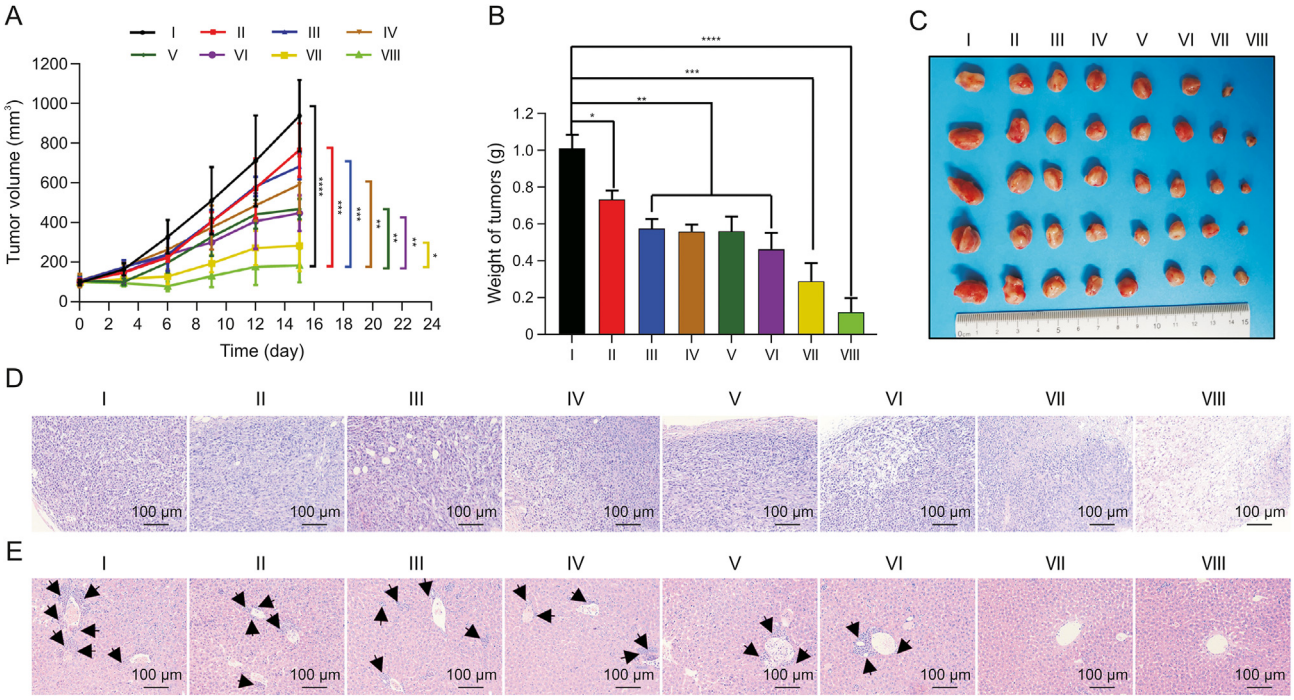

Fig. 7. Evaluation of *in vivo* antitumor efficacy of metformin (Met)–glucose oxidase (GOx)/Fe@epigallocatechin gallate (EGCG)-conjugated low-molecular-weight chitosan (LC-EGCG, LE) nanoparticles (NPs). (A, B) The relative tumor volume (A) and tumor weight (B) of 4T1 tumor-bearing mice treated with different formulations ($n = 6$). (C) The digital photos of tumors extracted from mice after different treatments for 15 days. (D) Histological observation of the tumor tissues with hematoxylin-eosin staining (H&E) staining from different treatment groups of mice. (E) Histopathologic profiles of liver treated with different drug formulations. The black arrow shows the liver metastases of breast cancer. I: control; II: Fe@LE NPs; III: Met; IV: GOx; V: Met + GOx; VI: Met/Fe@LE NPs; VII: GOx/Fe@LE NPs; and VIII: Met–GOx/Fe@LE NPs. $^{*}P < 0.05$, $^{**}P < 0.01$, $^{***}P < 0.001$, and $^{****}P < 0.0001$.

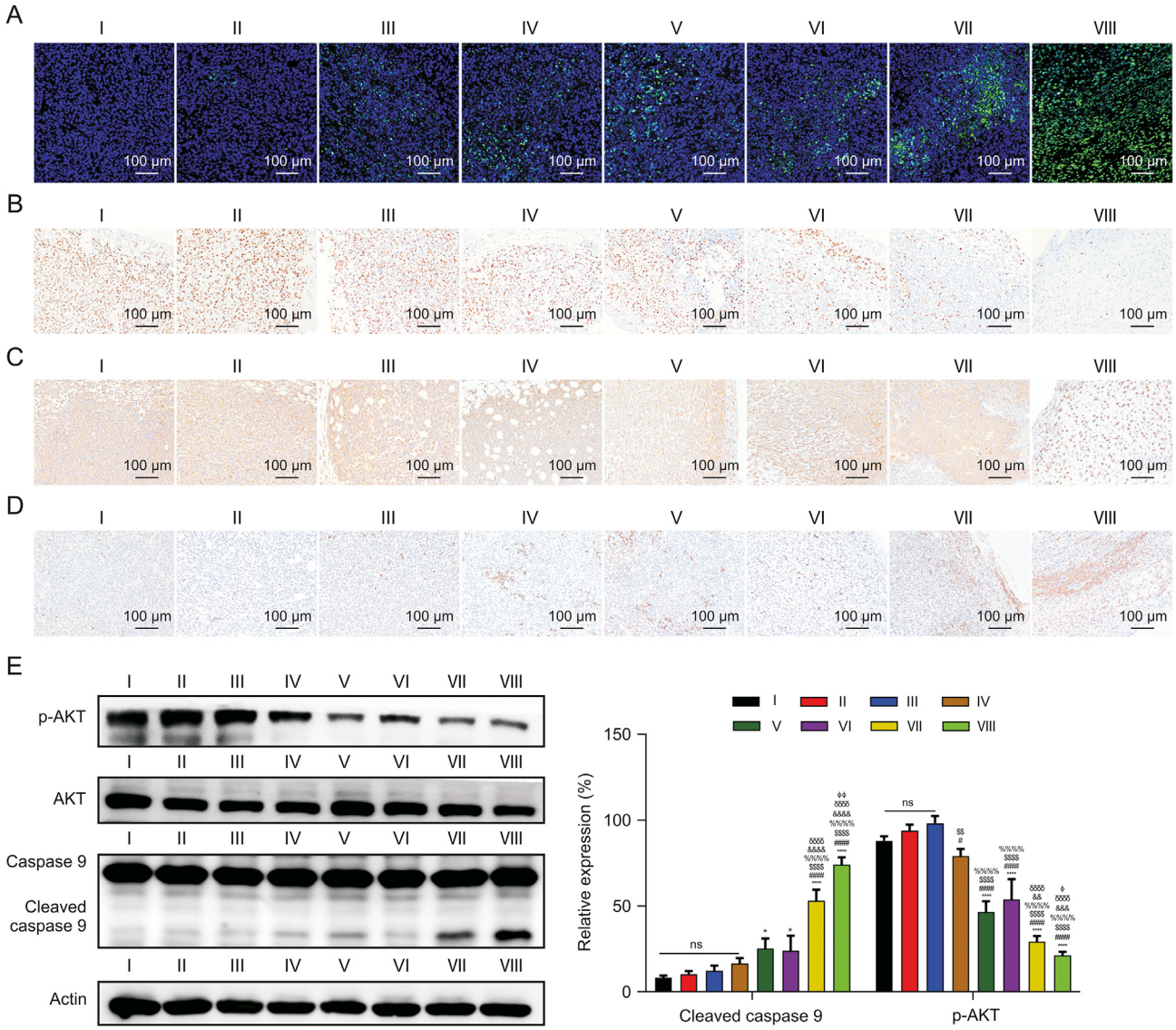

Fig. 8. *In vivo* anticancer mechanism of metformin (Met)–glucose oxidase (GOx)/Fe@epigallocatechin gallate (EGCG)-conjugated low-molecular-weight chitosan (LC-EGCG, LE) nanoparticles (NPs). (A–D) The terminal dexynucleotidyl transferase (TdT)-mediated dUTP nick-end labeling (TUNEL) immunofluorescent (A), Ki67 (B), caspase 9 (C), and cleaved caspase 9 (D) immunohistochemical staining of tumor slices. (E) Western blot analysis of cleaved caspase 9 and p-AKT after different treatments and the corresponding semiquantitative analysis by Image J. $^{*}P < 0.05$ and $^{****}P < 0.0001$ vs. group I; $^{\#}P < 0.05$ and $^{\#\#\#\#}P < 0.0001$ vs. group II; $^{\$\$}P < 0.01$ and $^{\$\$\$\$}P < 0.0001$ vs. group III; $^{\%\%\%\%}P < 0.0001$ vs. group IV; $^{\&\&}P < 0.01$, $^{\&\&\&}P < 0.001$, and $^{\&\&\&\&}P < 0.0001$ vs. group V; $^{\delta\delta\delta\delta}P < 0.0001$ vs. group VI; $^{\Phi}P < 0.05$ and $^{\Phi\Phi}P < 0.01$ vs. group VII. I: control; II: Fe@LE NPs; III: Met; IV: GOx; V: Met + GOx; VI: Met/Fe@LE NPs; VII: GOx/Fe@LE NPs; and VIII: Met–GOx/Fe@LE NPs. ns: no significance.

Fe@LE NPs significantly enhanced the content of cleaved caspase 9 (Figs. 8D and E), further demonstrating that this metabolism disruption and glucose starvation therapeutic strategy efficiently leads to apoptosis. The measured ATP levels after different treatments further prove that Met–GOx/Fe@LE NPs can impair ATP production (Fig. S12). As shown in Fig. S13, immunofluorescence staining of ROS was performed after different treatments to determine the generation of ROS in the tumor [4]. Compared with the control group, the ROS immunofluorescence in the Fe@LE NPs, Met, and GOx/Fe@LE NPs groups showed no significant changes, whereas the ROS immunofluorescence in the GOx, GOx + Met, GOx/Fe@LE NPs, and Met–GOx/Fe@LE NPs groups increased to different degrees, consistent with the results *in vitro* (Fig. 5C). These results collectively validated that the Met–GOx/Fe@LE NPs could efficiently inhibit tumor growth with negligible side effects and would be a powerful CS-based therapeutic agent for tumor therapy.

4. Conclusion

In summary, we successfully fabricated pH-responsive CS-EGCG nanocarriers (Met–GOx/Fe@LE NPs) for metabolism destruction/starvation/chemodynamic triple-combination therapy. As a CS-based nanocarrier, the positively charged amino groups of CS in the Met–GOx/Fe@LE NPs may interact with negatively charged biological membranes to enhance endocytosis by cells. The experimental results suggested that this nanocarrier could effectively accumulate in the tumor site and significantly inhibit tumor cell proliferation/metastasis by starvation-enhanced Met therapy, resulting in the complete destruction of tumors. Met–GOx/Fe@LE NPs could block the glucose metabolism pathway and accelerate Warburg effect damage to promote cell apoptosis. By introducing GOx, Met–GOx/Fe@LE NPs can significantly increase the ROS levels and decrease the intracellular pH of 4T1 cells. As a result, enhanced

Met-induced tumor metabolism destruction by GOx for triple-combination therapy was achieved. Such a destruction/starvation/chemodynamic triple-combination therapeutic strategy may open new avenues for efficient and specific cancer treatment.

CRediT anthor statement

Rangrang Fan: Conceptualization, Methodology, Data curation, Writing - Original draft preparation, Funding acquisition; **Linrui Cai:** Methodology, Investigation, Data curation; **Hao Liu:** Validation, Methodology; **Hongxu Chen:** Validation, Writing - Reviewing and Editing, Funding acquisition; **Caili Chen:** Writing - Reviewing and Editing; **Gang Guo:** Resources, Conceptualization, Formal analysis; **Jianguo Xu:** Resources, Writing - Reviewing and Editing, Supervision, Funding acquisition.

Declaration of competing interest

The authors declare that there are no conflicts of interest.

Acknowledgments

This study was supported by the National Natural Science Foundation of China (Grant Nos.: 82102767 and 82002655), the 1·3·5 Project for Disciplines of Excellence-Clinical Research Incubation Project, West China Hospital, Sichuan University, China (Grant No.: 2020HXFH036), the Knowledge Innovation Program of the Chinese Academy of Sciences, China (Grant No.: JH2022007), the Cultivation Project of Basic Medical College of Xinxiang Medical University, China (Grant No.: JCYXYKY202112), and the Key Project of Science and Technology of Henan Province, China (Grant No.: 222102310260).

Appendix A. Supplementary data

Supplementary data to this article can be found online at https://doi.org/10.1016/j.jpha.2023.09.015.

References

[1] Y. Liu, J. Ge, Y. Chen, et al., Combined single-cell and spatial transcriptomics reveal the metabolic evolvement of breast cancer during early dissemination, Adv. Sci. (Weinh.) 10 (2023), e2205395.
[2] H. Zhao, Y. Li, H. Shi, et al., Prodrug nanoparticles potentiate tumor chemo-immunometabolic therapy by disturbing oxidative stress, J. Control. Release 352 (2022) 909–919.
[3] X. Zhang, F. Luo, S. Luo, et al., Transcriptional repression of aerobic glycolysis by OVOL2 in breast cancer, Adv. Sci. (Weinh.) 9 (2022), e2200705.
[4] X. Meng, Z. Lu, Q. Lv, et al., Tumor metabolism destruction via metformin-based glycolysis inhibition and glucose oxidase-mediated glucose deprivation for enhanced cancer therapy, Acta Biomater. 145 (2022) 222–234.
[5] M. Mascaraque-Checa, M. Gallego-Rentero, J. Nicolás-Morala, et al., Metformin overcomes metabolic reprogramming-induced resistance of skin squamous cell carcinoma to photodynamic therapy, Mol. Metab. 60 (2022), 101496.
[6] J. Wan, S. Xu, J. Li, et al., Facile synthesis of multifunctional pharmaceutical carbon dots for targeted bioimaging and chemotherapy of tumors, Nanoscale 14 (2022) 11359–11368.
[7] D. Tailor, C.C. Going, A. Resendez, et al., Novel Aza-podophyllotoxin derivative induces oxidative phosphorylation and cell death via AMPK activation in triple-negative breast cancer, Br. J. Cancer 124 (2021) 604–615.
[8] W. Feng, W. Shi, Z. Wang, et al., Enhancing tumor therapy of Fe(III)-shikonin supramolecular nanomedicine via triple ferroptosis amplification, ACS Appl. Mater. Interfaces 14 (2022) 37540–37552.
[9] C. Zhu, Q. Ma, L. Gong, et al., Manganese-based multifunctional nanoplatform for dual-modal imaging and synergistic therapy of breast cancer, Acta Biomater. 141 (2022) 429–439.
[10] G. Zhou, M. Li, Near-infrared-II plasmonic trienzyme-integrated metal-organic frameworks with high-efficiency enzyme cascades for synergistic trimodal oncotherapy, Adv. Mater. 34 (2022), e2200871.
[11] H. Wen, Y. Fei, R. Cai, et al., Tumor-activatable biomineralized nanotherapeutics for integrative glucose starvation and sensitized metformin therapy, Biomaterials 278 (2021), 121165.
[12] J. Zhang, C. Liang, Z. Wei, et al., TME-triggered $MnSiO_3$@Met@GO_x nanosystem for ATP dual-inhibited starvation/chemodynamic synergistic therapy, Biomaterials 287 (2022), 121682.
[13] J. Gao, J. Wen, D. Hu, et al., Bottlebrush inspired injectable hydrogel for rapid prevention of postoperative and recurrent adhesion, Bioact. Mater. 16 (2022) 27–46.
[14] R. Fan, D. Chuan, H. Hou, et al., Development of a hybrid nanocarrier-recognizing tumor vasculature and penetrating the BBB for glioblastoma multi-targeting therapy, Nanoscale 11 (2019) 11285–11304.
[15] M. Mu, X. Liang, D. Chuan, et al., Chitosan coated pH-responsive metal-polyphenol delivery platform for melanoma chemotherapy, Carbohydr. Polym. 264 (2021), 118000.
[16] Q. Jin, W. Zhu, J. Zhu, et al., Nanoparticle-mediated delivery of inhaled immunotherapeutics for treating lung metastasis, Adv. Mater. 33 (2021), e2007557.
[17] B. Huang, M. Chen, J. Tian, et al., Oxygen-carrying and antibacterial fluorinated nano-hydroxyapatite incorporated hydrogels for enhanced bone regeneration, Adv. Healthc. Mater. 11 (2022), e2102540.
[18] E. Rosella, N. Jia, D. Mantovani, et al., A microfluidic approach for development of hybrid collagen-chitosan extracellular matrix-like membranes for on-chip cell cultures, J. Mater. Sci. Technol. 63 (2021) 54–61.
[19] O.U. Akakuru, C. Xu, C. Liu, et al., Metal-free organo-theranostic nanosystem with high nitroxide stability and loading for image-guided targeted tumor therapy, ACS Nano 15 (2021) 3079–3097.
[20] B.N. Kumara, R. Shambhu, A. Prabhu, et al., Novel chitosan-graphene quantum dots composite for therapeutic delivery and tracking through enzymatic stimuli response, Carbohydr. Polym. 289 (2022), 119426.
[21] S. Li, Y. Zhang, S.H. Ho, et al., Combination of tumour-infarction therapy and chemotherapy via the co-delivery of doxorubicin and thrombin encapsulated in tumour-targeted nanoparticles, Nat. Biomed. Eng. 4 (2020) 732–742.
[22] Y. Liang, Z. Li, Y. Huang, et al., Dual-dynamic-bond cross-linked antibacterial adhesive hydrogel sealants with on-demand removability for post-wound-closure and infected wound healing, ACS Nano 15 (2021) 7078–7093.
[23] N.K. Verma, A.K. Kar, A. Singh, et al., Control release of adenosine potentiate osteogenic differentiation within a bone integrative EGCG-*g*-NOCC/collagen composite scaffold toward guided bone regeneration in a critical-sized calvarial defect, Biomacromolecules 22 (2021) 3069–3083.
[24] J. Zhao, A. Blayney, X. Liu, et al., EGCG binds intrinsically disordered N-terminal domain of p53 and disrupts p53-MDM2 interaction, Nat. Commun. 12 (2021), 986.
[25] Z. Zhou, K. Li, L. Shi, et al., Self-assembled integrative nutrient carrier platform containing green tea catechin for short bowel syndrome treatment, Adv. Healthc. Mater. 12 (2023), e2201933.
[26] B. Zhang, R. Yao, C. Hu, et al., Epigallocatechin gallate mediated sandwich-like coating for mimicking endothelium with sustained therapeutic nitric oxide generation and heparin release, Biomaterials 269 (2021), 120418.
[27] C. Cieuta-Walti, A. Cuenca-Royo, K. Langohr, et al., Safety and preliminary efficacy on cognitive performance and adaptive functionality of epigallocatechin gallate (EGCG) in children with Down syndrome. A randomized phase Ib clinical trial (PERSEUS study), Genet. Med. 24 (2022) 2004–2013.
[28] L. Bu, C. Bi, Z. Shi, et al., Significant enhancement on ferrous/persulfate oxidation with epigallocatechin-3-gallate: Simultaneous chelating and reducing, Chem. Eng. J. 321 (2017) 642–650.
[29] H. Shi, R. Wang, H. Cao, et al., A metal-polyphenol-based oxygen economizer and Fenton reaction amplifier for self-enhanced synergistic photothermal/chemodynamic/chemotherapy, Adv. Healthc. Mater. 12 (2023), e2300054.
[30] F. Lei, X. Wang, C. Liang, et al., Preparation and functional evaluation of chitosan-EGCG conjugates, J. Appl. Polym. Sci. 131 (2014), 39732.
[31] J. Moellmann, S. Grimme, DFT-D3 study of some molecular crystals, J. Phys. Chem. C 118 (2014) 7615–7621.
[32] R. Fan, C. Chen, J. Hu, et al., Multifunctional gold nanorods in low-temperature photothermal interactions for combined tumor starvation and RNA interference therapy, Acta Biomater. 159 (2023) 324–337.
[33] L. Zhang, S. Wan, C. Li, et al., An adenosine triphosphate-responsive autocatalytic Fenton nanoparticle for tumor ablation with self-supplied H_2O_2 and acceleration of Fe(III)/Fe(II) conversion, Nano Lett. 18 (2018) 7609–7618.
[34] M. Mu, H. Chen, R. Fan, et al., A tumor-specific ferric-coordinated epigallocatechin-3-gallate cascade nanoreactor for glioblastoma therapy, J. Adv. Res. 34 (2021) 29–41.
[35] M. Wu, Q. Wang, S. Chen, et al., Metabolic intervention liposome for targeting glutamine-addiction of breast cancer, J. Control. Release 350 (2022) 1–10.
[36] Z. Mo, X. Pan, X. Pan, et al., MOF(Fe)-derived composites as a unique nanoplatform for chemo-photodynamic tumor therapy, J. Mater. Chem. B 10 (2022) 8760–8770.
[37] Q. Zheng, Y. Fang, L. Zeng, et al., Cytocompatible cerium oxide-mediated antioxidative stress in inhibiting ocular inflammation-associated corneal neovascularization, J. Mater. Chem. B 7 (2019) 6759–6769.
[38] R. Fan, C. Chen, H. Hou, et al., Tumor acidity and near-infrared light responsive dual drug delivery polydopamine-based nanoparticles for chemo-photothermal therapy, Adv. Funct. Mater. 31 (2021), 2009733.
[39] M. Miao, L. Mu, S. Cao, et al., Dual-functional CDs@ZIF-8/chitosan luminescent film sensors for simultaneous detection and adsorption of tetracycline,

Carbohydr. Polym. 291 (2022), 119587.
[40] W. Ni, J. Wu, Y. Feng, et al., Metformin reprograms tumor microenvironment and boosts chemoimmunotherapy in colorectal cancer, Biomater. Sci. 10 (2022) 5596–5607.
[41] W. Zhou, X. Tang, J. Huang, et al., Dual-imaging magnetic nanocatalysis based on Fenton-like reaction for tumor therapy, J. Mater. Chem. B 10 (2022) 3462–3473.
[42] Y. Zhang, S. Jiang, J. Lin, et al., Antineoplastic enzyme as drug carrier with activatable catalytic activity for efficient combined therapy, Angew. Chem. Int. Ed. Engl. 61 (2022), e202208583.
[43] N. Hashemifard, A. Mohsenifar, B. Ranjbar, et al., Fabrication and kinetic studies of a novel silver nanoparticles-glucose oxidase bioconjugate, Anal. Chim. Acta 675 (2010) 181–184.
[44] X. Li, Q. Zhou, A.A.M.M. Japir, et al., Protein-delivering nano complexes with Fenton reaction-triggered cargo release to boost cancer immunotherapy, ACS Nano 16 (2022) 14982–14999.
[45] T. Lu, Q. Chen, Independent gradient model based on Hirshfeld partition: A new method for visual study of interactions in chemical systems, J. Comput. Chem. 43 (2022) 539–555.
[46] T. Lu, F. Chen, Multiwfn: A multifunctional wavefunction analyzer, J. Comput. Chem. 33 (2012) 580–592.
[47] W. Humphrey, A. Dalke, K. Schulten, VMD: Visual molecular dynamics, J. Mol. Graph. 14 (1996) 33–38.
[48] L. Tan, J. Peng, Q. Zhao, et al., A novel MPEG-PDLLA-PLL copolymer for docetaxel delivery in breast cancer therapy, Theranostics 7 (2017) 2652–2672.
[49] E. Kirbas Cilingir, E.S. Seven, Y. Zhou, et al., Metformin derived carbon dots: Highly biocompatible fluorescent nanomaterials as mitochondrial targeting and blood-brain barrier penetrating biomarkers, J. Colloid Interface Sci. 592 (2021) 485–497.
[50] Z. Fan, T. Ren, Y. Wang, et al., Aβ-responsive metformin-based supramolecular synergistic nanodrugs for Alzheimer's disease via enhancing microglial Aβ clearance, Biomaterials 283 (2022), 121452.
[51] J. Ren, L. Zhang, J. Zhang, et al., Light-activated oxygen self-supplied starving therapy in near-infrared (NIR) window and adjuvant hyperthermia-induced tumor ablation with an augmented sensitivity, Biomaterials 234 (2020), 119771.
[52] X. Meng, L. Chen, R. Lv, et al., A metal-phenolic network-based multifunctional nanocomposite with pH-responsive ROS generation and drug release for synergistic chemodynamic/photothermal/chemo-therapy, J. Mater. Chem. B 8 (2020) 2177–2188.
[53] M. Qian, Z. Cheng, G. Luo, et al., Molybdenum diphosphide nanorods with laser-potentiated peroxidase catalytic/mild-photothermal therapy of oral cancer, Adv. Sci. (Weinh.) 9 (2022), 2101527.
[54] Z. Liu, S. Liu, B. Liu, et al., Fe(III)-naphthazarin metal-phenolic networks for glutathione-depleting enhanced ferroptosis-apoptosis combined cancer therapy, Small 19 (2023), e2207825.
[55] D. Chuan, H. Hou, Y. Wang, et al., Multifunctional metal-polyphenol nanocomposite for melanoma targeted photo/chemodynamic synergistic therapy, J. Mater. Sci. Technol. 152 (2023) 159–168.
[56] R. Jaquish, A.K. Reilly, B.P. Lawson, et al., Immobilized glucose oxidase on magnetic silica and alumina: Beyond magnetic separation, Int. J. Biol. Macromol. 120 (2018) 896–905.
[57] Y. Zeng, H. Zhou, J. Ding, et al., Cell membrane inspired nano-shell enabling long-acting glucose oxidase for melanoma starvation therapy via microneedles-based percutaneous delivery, Theranostics 11 (2021) 8270–8282.
[58] N. Bertrand, J. Wu, X. Xu, et al., Cancer nanotechnology: The impact of passive and active targeting in the era of modern cancer biology, Adv. Drug Deliv. Rev. 66 (2014) 2–25.
[59] X. Ding, M. Liu, Q. Cheng, et al., Multifunctional liquid metal-based nanoparticles with glycolysis and mitochondrial metabolism inhibition for tumor photothermal therapy, Biomaterials 281 (2022), 121369.
[60] L. Dai, M. Yao, Z. Fu, et al., Multifunctional metal-organic framework-based nanoreactor for starvation/oxidation improved indoleamine 2,3-dioxygenase-blockade tumor immunotherapy, Nat. Commun. 13 (2022), 2688.
[61] X. Xu, Y. Ran, C. Huang, et al., Glucose and H_2O_2 dual-responsive nano complex grafted with insulin prodrug for blood glucose regulation, Biomacromolecules 23 (2022) 1765–1776.
[62] M. Mascaraque, P. Delgado-Wicke, C. Nuevo-Tapioles, et al., Metformin as an adjuvant to photodynamic therapy in resistant basal cell carcinoma cells, Cancers 12 (2020), 668.
[63] Y. Jiang, Y. Tan, K. Xiao, et al., pH-regulating nanoplatform for the "double channel chase" of tumor cells by the synergistic cascade between chlorine treatment and methionine-depletion starvation therapy, ACS Appl. Mater. Interfaces 13 (2021) 54690–54705.
[64] Q. Mu, G. Lin, Z.R. Stephen, et al., *In vivo* serum enabled production of ultrafine nanotherapeutics for cancer treatment, Mater. Today (Kidlington) 38 (2020) 10–23.